

**STEREO-VIDEO OBSERVATION OF NEARSHORE BEDFORMS
ON A LOW ENERGY BEACH**

20/2/01

JEFFREY S. DOUCETTE*

EUAN S. HARVEY**

&

MARK R. SHORTIS***

***DEPARTMENT OF GEOGRAPHY
UNIVERSITY OF WESTERN AUSTRALIA
CRAWLEY WA 6009 AUSTRALIA**

Phone: (61 8) 930-2651
Fax: (61 8) 9380-1054
jdoucett@gis.uwa.edu.au

****DEPARTMENT OF BOTANY
UNIVERSITY OF WESTERN AUSTRALIA
CRAWLEY WA 6009 AUSTRALIA**

*****DEPARTMENT OF GEOMATICS
UNIVERSITY OF MELBOURNE
PARKVILLE VIC 3052 AUSTRALIA**

ABSTRACT

A new technique utilising underwater stereo-video was tested for its ability to measure nearshore bed morphology at high-frequency and high-resolution. A stereo-video system was used to monitor small-scale ripple morphology (wavelengths 0.05m-0.10m, heights ~ 5mm) in the nearshore of a low-energy beach in south western Australia. Waves, currents and suspended sediment concentrations were also monitored.

Bed morphology could be measured with a mean accuracy of 2mm with the stereo-video system. Measurements in the field were limited to ripple crest positions since targets over the entire ripple profiles could not be identified in both the left and right stereo images. This could be overcome in the future by the use of laser stripes to illuminate the profiles and the generation of epipolar lines within the analysis software to match corresponding targets in each of the images. Ripple crest positions were measured at 1Hz and the relationship between ripple movement and near-bed hydrodynamics was investigated.

Ripple crests were found to oscillate at the same frequencies as the swell and wind waves. The magnitude of the ripple oscillation was much greater due to the swell waves than the wind waves. The ripples experienced net onshore migration that corresponded with onshore wave asymmetry, very small mean cross-shore currents and net onshore suspended sediment flux at 0.05m.

Keywords

bedforms, photogrammetry, low-energy environment, nearshore environment

1. INTRODUCTION

At present there is a lack of high-resolution measurement of bedforms, both in planform and profile, at frequencies approaching those at which the hydrodynamics are measured. High-frequency measurements of bedforms are needed to be able to relate driving forces to bed response since small-scale bedforms can change significantly under individual waves (Hanes et al., 1998). The nature of this change is not fully understood. An understanding of small-scale, both temporal and spatial, bedform dynamics is important for bedform/roughness prediction in suspended sediment transport modelling. One of the reasons for the lack of detailed observations of bedform dynamics is the difficulty in performing non-intrusive high-resolution measurements in the adverse nearshore conditions.

The aim of this paper is to evaluate the usefulness of stereo-video techniques for high-frequency measurement of bed profile and planform in the nearshore of a low energy beach. More specific objectives include the measurement of changes in ripple position over time and to relate ripple position changes, including oscillatory and net ripple movement, to the hydrodynamics.

A new technique utilising stereo-video was tested for its ability to perform high-frequency and high-resolution measurements of bed morphology. Video based techniques have been used for many qualitative and quantitative observations in studies of coastal processes. Video has been used in studies of beach profile (Plant and Holman, 1997), bedforms (Boyd et al., 1988; Crawford and Hay, 1998; Black and Oldman, 1999), boundary layers (Conley and Inman, 1992), grain size distributions (Foti and Blondeaux, 1995), sand bars (Lippmann and Holman, 1989; 1990; Lippmann et al., 1993), wave run-up (Holman and Guza, 1984; Holman and Sallenger, 1985; Aagaard and Holm, 1989; Holland et al., 1995), ripple migration (Li et al., 1997; Amos et al, 1999), and sediment transport thresholds (Davies, 1985; Li and Amos, 1999). Stereo-video techniques have been used successfully in marine studies for fast and accurate measurements of the size of swimming sharks (Klimley and Brown, 1983), area of intertidal communities (Whorff and Griffing, 1992), size of subtidal organisms (Harvey and Shortis, 1996), foreshore topography (Holland and Holman, 1997) and the growth of coral (Done, 1981). These studies demonstrate the

suitability of stereo-video for accurate high-frequency three-dimensional non-intrusive measurement underwater. Stereo-photography has been used by Kachel and Sternberg (1971) to measure ripple migration rates and heights, but the use of photography rather than video, limits the sampling interval.

Stereo-video techniques are based on the principle of stereo-photogrammetry. If two photographs of an image are taken at slightly different angles then it is possible to perceive depth from them. Similarly, a pair of underwater digital video cameras can be oriented at slightly different angles towards the same target and 24 images per second can be recorded by each camera to give 24 pairs of images or stereo-pairs. Once the field of view is calibrated, three-dimensional measurements can be made within the overlapping portion of the field of view within the stereo-pairs (eg. Harvey and Shortis, 1996). This technique has the potential to provide both elevation and planform observations of bedforms in a marine environment.

Current techniques for bedform observation appear to involve a trade-off between high-frequency measurements and large spatial coverage. Acoustic Backscatter Sensors (ABS) are able to make very high-frequency measurement of the bed elevation but are limited to observing a 'footprint' of several centimetres when oriented vertically (eg. Hanes et al., 1988; Osborne and Vincent, 1993; Villard et al. 2000). An additional ABS is needed to obtain ripple wavelength information. This is oriented in a sidescan mode although bedform heights cannot be obtained from this orientation. Track mounted sonar profiles work quite well in the nearshore, but they are limited to two-dimensional measurements and each profile takes several seconds to several minutes to complete depending on the detail required (Dingler et al. 1977; Greenwood et al., 1993). Crawford and Hay (1998) used a video/laser system that was capable of much higher frequency measurements than the track mounted sonars. The measurements were limited to two-dimensional profiles although additional systems could be oriented at different angles. Side-scan (Thornton et al., 1998) and rotary sonar (Hay and Wilson, 1994) have been used to obtain information on the larger planform of the bed. These techniques provide coverage over large areas of the bed but measurements are time consuming. For example, Hay and Wilson's (1994) rotatory sonar observes 10 m^2 of the bed although one scan takes 47s to perform.

These techniques are not capable of height measurements so additional instruments are needed to obtain a three-dimensional impression of the bed. Measurement of ripple heights and wavelengths are possible with single video cameras as used by Boyd et al. (1988) and Li et al. (1997) but it is difficult to measure in three-dimensions as accurately as with stereo-video.

2. STEREO-VIDEO SYSTEM

2.1 Equipment

Image recording for the stereo-video analysis was performed with 2 Sony DCR-TRV900E digital video camera recorders in custom made waterproof housings. The cameras were powered by the standard supplied battery (NP-F330), which gave a continuous recording time of 70min. Standard mini DV cassettes were used. This limited the recording time to approximately 50min. The cameras also have the ability to record for 0.5s to 2s at intervals of 30s to 10min if a longer period of observation is required.

The cameras were mounted at an inwardly converging angle of 8.1 degrees on a base bar 0.25m apart (Fig. 1). Focal length of the cameras was 3.45mm in water. This configuration gave an overlapping field of view of 0.59m x 0.47m at a distance of 0.6m. The relative camera angle chosen is a trade off between field of view and measurement precision. A more acute convergence would decrease the useable field of view, but improve the measurement precision (Harvey and Shortis, 1996).

A light emitting device was mounted approximately 0.2m in front of the cameras. The device was oriented facing the cameras and within the field of view of both the cameras. It consisted of a ring of small lights which flashed in sequence at greater than 24Hz. This was used to synchronise the individual images or frames from the left and right cameras since the internal clocks in each camera may not have been fully synchronised and the synchronisation may drift over long duration recording. The pairing of the stereo-images must be exact to avoid motion parallax from either movement of the cameras or the objects to be measured. The light emitting device could be manually operated, which was essential for image synchronisation during calibration. The paired images are captured from the digital tapes using DV Raptor

video software (Canopus Corporation). Images were chosen by looking at the recording frame-by-frame. The captured images were saved in a Tagged Image File Format (.tif) and were 1217KB in size.

2.2 Camera Calibration

Following is a summary of the calibration procedure explained in more detail by Harvey and Shortis (1996). Calibration of the stereo-video system can be divided into two parts. First the internal geometric characteristics of the cameras, which is known as camera calibration are determined. Camera calibration involves determining physical parameters of principal point position, principal distance, the effects of radial and decentring lens distortions, the effects of refraction at the air-glass and glass-water interfaces and any bias in the spacing of the pixels on the CCD (charge-coupled device) sensor. Second the relative orientation of the cameras is established. This requires parameters to define the separation of the perspective centres of the cameras on the base bar, the angle of the cameras optical axes and the rotations of one camera with respect to the other.

Camera and relative orientation calibration are determined by *in situ* self calibration of the cameras using a three dimensional control frame (Harvey and Shortis, 1996). The control frame used here was a black open 0.4m x 0.4m x 0.4m cube with 108 white dots spread over the frame (Fig. 2). These were easily discernible targets in each of the stereo-pair images. Other unique white shapes were painted on the frame to be used for identification of the frame orientation and semi-automation of the calibration process.

The calibration frame was filmed in 5 different orientations (facing camera at 45 degrees and rotated though 4 quarter turns, and one at 90 degrees to the camera) and 4 different camera positions (right side up, upside down, vertical left and right) resulting in 20 stereo image pairs for calibration. Different camera positions were used to decouple some of the parameters of self-calibration. The procedure takes several minutes and can be performed in the outer edge of the surf zone without the aid of scuba. Only approximate target coordinates are needed for subsequent calibrations so the calibration frame does not need to maintain its exact shape between calibrations.

The frame only has to maintain its shape for the duration of the image acquisition during *in situ* calibration.

Location of the targets on the frame were identified in each of the 20 synchronised pairs using the Vision Measurement System (VMS) software. This involved selecting a minimum of four targets manually in each image to determine the initial estimates of the location and orientation of the exposure station relative to the calibration frame. The process was then completed by the automatic measurement of all remaining targets on the calibration frame for each image, based on their known positions on the frame. The location of the targets, target image measurements and exposure station data was used as input into a self-calibrating multi-station bundle solution (Granshaw, 1980) implemented within VMS. The bundle solution calculates the estimates and precisions of the camera calibration parameters and the location and orientations of the exposure stations for each synchronised pair of images. Since the calibration images were recorded underwater where the measurements were to be made, factors such as housing geometry and the refractive index of the water are modelled implicitly in the calibration parameters.

The cameras were calibrated every time they were removed from their waterproof housing. There was a possibility of variation in the calibrations due to the instability of the internal properties of the camera and properties of the medium (Shortis et al., 2000). Digital still cameras have been shown to experience variations in calibration parameters due to the flexing of the body of the camera and the movement of the focal plane CCD sensor (Shortis and Beyer, 1997).

2.3 Testing the Calibration

The theoretical precision of object space measurements made with any stereo-video or stereophotogrammetric system is based on the precision of image measurement and the geometry of the stereo-pair. The simplest case is derived from the geometry of a stereo-pair with the optical axes of the cameras parallel to one another and perpendicular to the base vector between the perspective centres of the camera lenses. It can be shown that:

$$\sigma_x = \sigma_y = \frac{Z}{f} \sigma_i$$

$$\sigma_z = \frac{Z^2}{bf} \sqrt{2} \sigma_i$$

where σ_x , σ_y , σ_z are precisions in the X, Y, Z coordinate axes, Z is the camera to object separation in the depth direction parallel to the camera optical axes, f is the mean principal distance of the cameras, b is the base separation between the camera perspective centres and σ_i is the precision of measurement in the image space.

For a real underwater stereo-video system this ideal case will not be exactly replicated, however the departures from the ideal case are small. The precision estimators given above are a worst case scenario, given that the geometry of the stereo-video system is close to ideal and that the camera mountings provide a slight convergence of the camera optical axes.

The location in the X-Y plane is often considered to be a measurement of position, and the Z component is a measurement of depth or range. The clear distinction between the two precision estimators given above is that position measurement deteriorates linearly with distance away from the cameras, whereas depth measurement deteriorates in proportion to the square of the distance.

The precision and accuracy of the stereo-video system was tested in a laboratory water tank and in the field. Accuracy was tested by measuring known distances and heights in a water tank after *in situ* calibration of the system. Nails of different length were hammered into a board at random spacings. The board was placed on the bottom of the tank and images were recorded from several angles with the stereo-video system at an average range of 0.6m. Measurements were then made from the stereo-pairs and compared to the actual distances measured with callipers. Measurements were divided into 3-dimensions where z is the nail height and x and y describe the horizontal distances between the base of the nails. 30 measurements were made in each dimension and were repeated 5 times to establish the precision.

Measurement accuracy was also tested in the field after the field calibration. Measurements were made of known distances on the calibration cube. 30 measurements were made in each of the three dimensions. These were repeated 5 times to establish the precision. The results are discussed below.

3. FIELD SITE

Field observations were made at Port Beach, Perth, WA (Fig. 3), a low energy beach with average annual significant wave heights less than 1.0m. The beach is sheltered by Rottnest Is. and a chain of islands and reef between Rottnest Is. and Garden Is. The tidal regime is mixed, mainly diurnal with a spring-tide range of 0.9m (Department of Defence, 2000). Mean grain size at the time of observations was 0.26mm with a standard deviation of 0.13mm at 45m offshore. The sand was composed of a mixture of calcium carbonate and quartz. The water was very clear and provided excellent visibility for bedform observations except during exceptional suspension events.

Bed morphology consisted of plane bed close to shore that graded to patches of well-defined, but very flat, parallel crested ripples that would be termed small-scale post vortex ripples by Osborne and Vincent (1993). The patches of parallel ripples were within an area of irregular forms. The parallel ripples were oriented parallel to the wave crests and had wavelengths of 0.05-0.10m and heights of approximately 5mm.

Significant wave heights during the study were 0.44m. The water surface elevation record was divided into swell frequencies (0.05-0.15Hz) and wind wave frequencies (0.15-0.5Hz). Significant swell wave heights were 0.36m at 12s and wind wave heights were 0.24m at 4s. Longshore current was negligible at 0.02m/s.

4. FIELD METHODOLOGY

High-frequency measurements of waves, cross-shore and longshore currents and suspended sediment concentrations were obtained using a portable instrument pod. The pod consisted of 1 pressure sensor, 1 512 Marsh-McBirney electromagnetic current meter and 2 Optical Backscatter Sensors (OBS). The pressure sensor was

mounted at 0.10m and the current meter at 0.25m. The OBS were mounted at 0.05m and 0.13m. The instruments were suspended above the bed and were mounted a sufficient distance from the pod supports to minimise disturbance of flow or bedforms. All instruments were hard wired to shore and sampled at 4Hz for 50min.

The stereo-video system was mounted on a horizontal bar supported 0.5m above the bed by 2 triangular supports 2m apart (Fig. 1). The cameras were oriented to face directly down on the bed. The lens were 0.6m above the bed and the light emitting device was approximately 0.25m above the bed. This minimised any disturbance of the bedforms or flow field.

The instrument pod and the stereo-video system were deployed 45m from shore in 1.5m of water just outside the breaker zone. Five thin steel pegs (~0.5cm diameter) to be used as reference points were pushed into the bed at the edge of the field of view of the cameras.

5. RESULTS

5.1 Measurement Accuracy and Precision

In the water tank, measurements were most accurate along the x-axis where they were within an average of 0.6mm of the actual value and with little deviation (Fig. 4). This decreased slightly to just over 0.4mm after 4 further repetitive observations. Error bars in Figs. 4 and 5 denote the standard error. Average errors were slightly higher for the y-axis (up to 0.9mm), whereas the z-axis was the least accurate dimension with average errors up to 1.4mm.

Measurement of height was slightly less accurate in the field with mean errors of 2mm (Fig. 5). This accuracy increased with consecutive measurements to 1.4mm. The decrease in the accuracy of height in the field was likely a result of the greater heights measured in the field test. Heights measured in the field on the calibration frame were between 195mm and 280mm, whereas the nail heights measured in the water tank were only 16mm to 64mm. The greater range of heights in the field had a consequence that some measured locations were more distant from the cameras and, as the precision deteriorates with the square of the distance, the distant points will

generate a poorer result overall. The nail heights were closer to typical ripple heights and therefore should be considered more representative of the achievable accuracy.

The degree of precision was similar to the degree of accuracy. Theoretical calculations show that height measurements at a range of 0.6m will be precise to within 1.2mm (Table 1). The table is based on an image measurement precision of approximately 0.6 pixels, which is a value for manual pointing based on experience under optimal conditions. For the video cameras used, this corresponds to 3 micrometres on the CCD sensor. Along the x and y axes, length measurements should be precise to within 0.5mm. Measurements of the same distances along the x-axis varied by up to 2.4mm with an average variation of 1mm in the water tank. In the field, measurements of the same distances along the x-axis varied by up to 2mm with an average variation of 0.8mm. This was slightly higher along the y and z axes in both the water tank and the field.

5.2 Failure to measure Ripple Profiles

While measurements could be made in all three dimensions, normally within 2mm, it was not possible to measure ripple profiles using the current stereo-video system. Stereo-photogrammetry requires the identification of equivalent points on synchronised images from both the stereo-video cameras. This was very difficult over a uniform sandy bed since distinguishable points were not present over entire ripple profiles. Similar problems were encountered by Kachel and Sternberg (1971). The ripple crests were distinct and their position could be easily identified. Lateral positions along the crests were matched between the stereo-pairs by defining an axis through the centre of the field of view (perpendicular to the ripple crests) and equidistant from the small marker pegs at the edges of the observed area.

Profiles were measured over an artificial rippled surface in a water tank to test the ability of the system to measure ripple profiles when common points could be identified in each of the stereo-pairs. Dotted lines were drawn on an artificial ripple surface and images were recorded by the stereo-video system oriented vertically above the surface. The dotted lines provided targets that could be easily identified in each of the stereo-pairs. Profiles were measured using the stereo images and compared to the

actual profiles (Fig. 6). The profiles generated using the stereo-video system were very close to the actual profiles with maximum errors of approximately 3mm. This suggests that in future applications all that is needed to measure ripple profiles in the field are identifiable points on the ripples. Possible means of achieving this are given in the discussion.

5.3 Ripple crest positions over time

A total of 50min of hydrodynamic, suspended sediment and video data were recorded but only the last 26min of data were used in the subsequent analysis (Fig. 7). The first 24min of observations were not used in order to enable the bed to recover from any disturbances that occurred while the cameras were being deployed.

Positions of 3 ripple crests in the centre of the field of view were measured from the stereo-pairs every second (Fig. 7a). A sampling rate of only 1Hz for ripple measurement was chosen out of the available 24 frames per second as a trade off between resolution and analysis time. It was thought that 1Hz would capture the ripple movement in sufficient detail. Only 2 of the ripples were in the field of view for the entire period of observation due to the net onshore migration of the ripple field. Gaps in the time series occurred when the bed was obscured by suspended sediment.

There was no significant trend in wave heights or cross-shore currents (u) (Fig. 7b and c). Water level decreased slightly and suspended sediment concentration increased over time (Fig. 7b and d). The increase in suspended sediment concentration may have been due to the drop in water level but there was no corresponding increase in cross-shore velocities. Note that the crest positions fluctuate at similar frequencies as the water level and cross-shore currents.

5.3.1 Ripple response to cross-shore current

Spectral analysis was performed on 1028 seconds (4096 observations) of the cross-shore current time series. Unfortunately, the ripple position time series had missing values and these values were linearly interpolated before spectral analysis of 1028 seconds (1028 observations) of the time series. Both time series were Hann tapered and had 16 degrees of freedom. The spectrum of a shorter portion of the ripple

position record (128s), with very few interpolated points, was also calculated to establish the effect of the interpolated points (Fig. 8b). This short data set only had 4 degrees of freedom and was only used to show the relative height of the spectral peaks. For comparison, the spectrum of the same 128 second portion of the cross-shore current time series was also calculated with 8 degrees of freedom (Fig. 8a).

The cross-shore current spectrum shows distinct peaks at swell (14s) and wind wave (4.8s) frequencies. Peaks for the wind and swell waves shifted slightly for the shorter portion of the time series. The location of the spectral peaks of the cross-shore current and ripple position match for both the spectra of the long and short portions of the time series with two notable exceptions. First, the lack of a peak in the spectrum of the longer time series for the ripple crests at the wind wave frequency (0.2-0.25Hz). Second, the presence of a large peak in energy of the long ripple position time series at very low frequencies. The first can be partially attributed to the linear interpolation of missing points in the ripple position time series, which resulted in the smoothing of some high-frequency oscillations. Although, it can also be seen that there was proportionally less energy in the ripple position spectrum at wind wave frequencies of the shorter time series where very few data points were interpolated. The second was due to the presence of a very long period fluctuation in ripple crest position that was not apparent in either the cross-shore current record or the wave record (Fig. 7).

Co-spectral analysis was performed between 1028 seconds of the cross-shore current and ripple position time series (Fig. 8c). The cross-shore data were reduced to 1Hz to match the ripple position sampling frequency. The resulting co-spectrum had 16 degrees of freedom. The co-spectrum shows that the cross-shore current and ripple positions were positively correlated at all dominant frequencies.

Co-spectral analysis was also performed between the cross-shore current record and the suspended sediment concentration at 0.05m (Fig. 8d). Data series were 4096 observations long and Hann tapered with 16 degrees of freedom. Suspended sediment transport was onshore at the dominant swell wave frequencies. This mirrored the onshore movement of ripples at these frequencies. At wind wave frequencies there was mainly offshore transport. Offshore transport also occurred at frequencies greater

than the swell wave frequencies. This could be due to coupling of suspended sediment concentrations with the trough of the group bound long wave (Larsen, 1982; Shi and Larsen, 1984; Masselink and Pattiaratchi, 2000).

Further evidence to support the lack of ripple position fluctuation at wind wave frequencies can be seen in Fig. 9. This sample of the data series shows much larger fluctuations in ripple position at swell wave frequencies than at wind wave frequencies (Fig. 9a and b). The time series of ripple positions appears to be a smoothed version of the cross-shore current time series. While it appears there was very little movement of ripples at wind wave frequencies there was actually ripple movement at both the swell and wind wave frequencies (Fig. 9c and d). Cross-shore current and ripple position data sets were low pass filtered at 0.1Hz and the remaining fluctuations correlate quite well (Fig. 9c). The data sets were also high pass filtered at 0.2Hz (Fig. 9). The remaining time series show highly correlated fluctuations, which means the ripples were also moving at the same frequencies as the wind waves. The cross-shore currents at the swell frequencies were about one third higher than those at wind wave frequencies (swell $u_m = 0.40\text{m/s}$, sea $u_m = 0.29\text{m/s}$, where u_m is the maximum orbital velocity, 2σ), but the magnitude of the ripple movement was a factor of 3 lower at the wind wave frequencies than at the swell wave frequencies. There were also some occasions when the ripples did not move in response to some of the smaller wind waves. An example of this was at time 835s (Fig. 9d) where the ripple remained almost stationary suggesting that the threshold of ripple movement was not crossed.

5.3.2 Net Ripple Migration

Net onshore ripple migration occurred over the period of observation. This appears to be a result of the asymmetric and skewed cross-shore current record (Fig. 10a and c). Cross-shore velocity asymmetry was calculated as defined by Clifton (1976):

$$u_{\text{asym}} = u_{\text{on}} + u_{\text{off}}$$

where u_{on} and u_{off} are the maximum onshore and offshore velocities for each zero up-crossing of the cross-shore current record (Fig. 10a). Mean velocity asymmetry for the duration of observation was 0.06m/s onshore. The line of best fit on Fig. 10a shows that asymmetry decreased slightly over time. Mean cross-shore velocity skewness was also onshore and decreased slightly over time. Mean cross-shore current was calculated for each wave as defined by the zero up-crossing. Overall mean cross-shore current was insignificant (-0.006m/s) but varied substantially between waves. The line of best fit in Fig. 10b shows slightly onshore mean velocity that became slightly negative by the end of observations. This could be a result of the decrease in water level and the offshore movement of the breaker zone towards the instrument location.

The mean suspended sediment flux at 0.05m was directed offshore at $0.004\text{kg/m}^2\cdot\text{s}$. This amount was an order of magnitude smaller than the $0.03\text{kg/m}^2\cdot\text{s}$ onshore net flux (Fig. 10d). This shows that the stronger instantaneous onshore currents were more influential to the suspended sediment transport than small mean offshore current. All the largest transport events were directed onshore.

Mean ripple migration rate was onshore at 0.96cm/min (Fig. 10e). Net onshore movement of the ripple crests apparently was a result of the stronger onshore currents as shown by the onshore wave asymmetry and skewness and the net onshore suspended sediment flux at 0.05m.

6. DISCUSSION

Three-dimensional measurements could be made with the stereo-video system in the field, however measurement of ripple profiles was not possible. The system was capable of accurately measuring the heights of vertical nails in a board, widths of the nails and distances between nails. Theoretically it is capable of measuring ripple morphology. Ripple profiles could not be measured in the field because it was not possible to identify distinct points on the ripple profiles in each of the images comprising the stereo-pairs. Profiles over artificial ripples were measured with the aid of identifiable targets over the entire ripple profiles suggesting that profile

measurements could be made in the field if a means of identifying common points between the left and right stereo images is available.

Identification of the same points on each of the stereo-pairs could be accomplished in future experiments by a projected pattern of laser dots or stripes. A dot array could be used to uniquely and unambiguously identify matching points in the left and right images of the stereo pair. However, the density of the dot arrays available using laser gratings may not be sufficient for high accuracy surface definition. An alternative is to use laser stripes, which allow a data density limited by only the image resolution in the stripe direction. Matching left and right locations can be identified using crossing points of epipolar lines generated within VMS by the geometry of the stereo imagery. In either case there is the potential to compile a digital elevation model of the surface that can be subsequently used to study the evolution of ripple morphology.

The measurement accuracy of the stereo-video system for measuring dimensions of identifiable targets was as good or better than the accuracy of other current bedform monitoring systems. Crawford and Hay (1998)'s camera and diode laser system has an accuracy of 2mm when measuring artificial triangular ripples in the laboratory. The track mounted sonar device (HRRTS II) described in Greenwood et al. (1993) has a resolution of $\pm 0.001\text{m}$ in laboratory conditions. This increased to a few mm under field conditions where there was additional noise due to suspended sediment and air bubbles in the water column. ABS measurements of height are generally accurate to within 5mm (Hanes et al., 1988; Osborne and Vincent, 1993; Villard et al. 2000). Dingler and Inman (1976)'s track mounted sonar had a resolution of 1mm just outside the surf zone in conditions similar to those measured here.

The major limitation of the technique, like most video based techniques, is that it can only be used in high visibility environments. The current trend in development of systems for remote sensing of the bed focuses on techniques that can observe bedforms under high energy conditions when the bed is highly active but obscured by suspended sediment. It has been shown here that on low energy beaches the ripples can be highly mobile even when they are not obscured by suspended sediment. There

is a great deal that can be learned about ripple dynamics under such low energy conditions. This technique would also be ideal for measurements in deeper offshore shelf environments where energies at the bed can be similar to those found here. Crawford and Hay (1998)'s use of lasers to illuminate the bed overcomes some of the noise in the measurements due to suspended sediment, but the technique is limited to periods with low ambient light such as twilight or night time.

There are no previous studies of ripple position response to individual waves, to the author's knowledge. The only other established technique that allows the accurate measurement of ripple crest position at the frequencies of wave and cross-shore current measurement appears to be the laser-video system of Crawford and Hay (1998), which can be operated at up to 30 frames per second. Hence, it is not known whether or not there is a lag in the response of a rippled bed to the fluid flow. While exact lags could not be determined due to the uncertainty of the synchronisation of the hydrodynamic and video data (± 1 s), there was ripple movement at the same dominant frequencies as the cross-shore current. There was no lag in the maximum correlation between ripple crest position and cross-shore velocity at a resolution of ± 1 s. The ripple movement was also in phase with the cross-shore current at the dominant frequencies as shown by the positive peaks in the co-spectrum between cross-shore current and ripple movement.

Since bedload is difficult or nearly impossible to measure, ripple migration rate is often used as a surrogate for bedload (eg. Amos et al., 1999). The net onshore migration of ripples here suggests net onshore bedload transport. The fact that the ripples could be observed moving substantially during periods with very limited suspension suggest bedload is a large part of the cross-shore transport on low energy beaches. The ripples migrated in the same direction as the net suspended sediment transport as measured at 0.05m above the bed. Although net suspended sediment transport was onshore, there was some offshore transport at wind wave frequencies and at very low frequencies. It is possible that under the smaller wind waves there was only suspension under the stronger onshore phase of wave motion. This suspended sediment could then be carried offshore under the wave trough as described by Sleath (1982).

Swell and wind wave frequencies were present in the ripple position record as shown in Figs. 8 and 9, but the degree of variance at the wind wave frequencies were 3 times less than at the swell wave frequencies. The associated difference in the strength of the cross-shore currents at swell and wind wave frequencies was only 25%. There was an obvious non-linear response of the ripple movement to the cross-shore current. This supports previous models of bedload transport since bedload in uni-directional flows is generally related to some power function, generally cubic, of shear velocity (eg. Bagnold, 1954; Inman, 1963; Lettau and Lettau, 1978; Hanes and Bowen, 1985).

The net migration direction of these small-scale parallel ripples is apparently determined by the same factors controlling the migration of the larger-scale parallel ripples observed in Doucette (in review). Doucette (in review) found that the ripple migration direction was a result of the balance between the offshore mean current and the onshore current asymmetry and skewness. Ripples migrated onshore when there was relatively higher onshore current asymmetry and skewness and relatively lower offshore mean flow. When offshore mean flow increased and onshore current asymmetry decreased or even reversed, the net ripple migration was offshore. The former conditions were present in this study. The small-scale parallel ripples moved onshore with the positive current asymmetry and skewness and the very weak offshore mean flow. In the nearshore, Brander (1991) also found ripple migration related to cross-shore velocity skewness, but on the deeper shoreface, Boyd et al. (1988) found no consistent relationship to near-bed mean currents or near-bed velocity skewness. The tips of the crests of the larger scale ripples observed in Doucette (in review) oscillated under some individual waves similar to the movement of the entire ripples here. Unfortunately detailed observations at individual wave frequencies were not obtained in that study.

Mean ripple migration rate in this mainly oscillatory nearshore environment was 0.96cm/min onshore. This was slightly faster than rates measured for similar size bedforms by Brander (1991). His migration rates were 0.13-0.72cm/min for ripples with wavelengths between 8-12cm and heights of 0.42-0.95cm. Brander (1991)'s maximum migration rate was achieved under maximum near-bed orbital velocities of

1.24m/s and skewness values up to 0.30. Both his maximum near-bed orbital velocities and skewness were higher than those recorded here, but there were higher migration rates measured in this study. Brander (1991) migration rates may have been slightly slower since his ripples were slightly bigger than those measured here and there was an offshore mean current of 0.05m/s during his maximum onshore migration rate. This mean offshore flow may have worked against the onshore velocity skewness. Boyd et al. (1988) recorded much slower migration rates of 0.16cm/min but these were measured in a deeper shoreface environment. Other studies had higher migration rates for similar small-scale bedforms in nearshore environments. For example, Dinger and Inman (1976) recorded migration rates of up to 4.2cm/min and Osborne and Vincent (1993) recorded migration rates of up to 5cm/min. In the latter study, observations were made on a macro-tidal beach and bedform migration may have been accelerated by the changing water level. Doucette (in review) suggest that water level influences bedform migration direction and rate. In that paper, maximum migration rates of only 0.2cm/min were recorded for much larger parallel ripples. The lower migration rates were likely a result of the larger size of the bedforms, the coarser sand and the weaker onshore current asymmetry.

7. CONCLUSIONS

Stereo-video techniques were found to be capable of high-frequency accurate measurements of ripple crest positions. Artificial ripple profiles could be measured but field measurements of actual ripple profiles was limited by the lack of identifiable targets on the ripples. Potential techniques are available to overcome this problem in the future. The use of laser stripes and epipolar lines generated within VMS would allow matching of points in the left and right stereo pairs. A digital elevation model could then be produced with a sufficiently dense data set.

No lag was found in the maximum correlation between ripple crest position and cross-shore velocity at a resolution of ± 1 s. This suggests that small-scale ripples respond almost instantly to the near-bed shear stresses when the stresses are large enough to entrain sediment. The small-scale ripples observed here oscillated on and offshore at the same frequencies as the cross-shore current. While the ripples moved at both swell and wind wave frequencies, they moved 3 times further at swell wave

frequencies. The cross-shore currents due to swell waves were only approximately one third greater than those due to wind waves. This shows that there is a non-linear response of ripple position to the cross-shore current and that the degree of ripple movement is influenced by the frequency of the driving force.

Net onshore ripple migration of small-scale parallel ripples was a result of onshore cross-shore current asymmetry and skewness, and very weak offshore mean flow. These are the same conditions under which net onshore ripple migration was found for larger scale parallel ripples by Doucette (in review).

ACKNOWLEDGEMENTS

Jeff Doucette was supported by a NSERC post graduate scholarship for the duration of this work. Thanks to Ian Eliot for critical comments on the draft manuscript and to David Johnson for help in the field.

References

- Aagaard, T. and Holm, J., 1989. Digitisation of wave run-up using video records. *J. Coastal Res.* 5 (3), 547-551.
- Amos, C.L., Bowen, A.J., Huntley, D.A., Judges, J.T. and Li, M.Z., 1999. Ripple migration and sand transport under quasi-orthogonal combined flows on the Scotian Shelf. *J. Coastal Res.* 15 (1), 1-14.
- Bagnold, R.A., 1954. Experiments on a gravity-free dispersion of large solid sphere in a Newtonian fluid under shear. *Proc R. Soc. London A225*, 49-63.
- Black, K.P. and Oldman, J.W., 1999. Wave mechanisms responsible for grain sorting and non-uniform ripple distribution across two moderate-energy, sandy continental shelves. *Mar. Geol.* 162, 121-132.
- Boyd, R., Forbes, D.L. and Heffler, D.E., 1988. Time-sequence observations of wave formed sand ripples on an ocean shoreface. *Sedimentology* 35, 449-464.
- Brander, R.W., 1991. Bedform constraints on sediment re-suspension and transport under shoaling and breaking waves. Unpubl. M.Sc. thesis, University of Toronto, 173 pp.
- Clifton, H.E., 1976. Wave-formed sedimentary structures- a conceptual model. In: *Beach and Nearshore Sedimentation* (ed. By R.A. Davis Jr. and R.L. Ethington). *Spec. Publs. Soc. Econ. Paleont. Miner.*, Tulsa, 24, 126-148.
- Conley, D.C. and Inman, D.L., 1992. Field observations of the fluid-granular boundary layer under near-breaking waves. *J. Geophys. Res.* 97 (C6), 9631-9643.
- Crawford, A.M. and Hay, A.E., 1998. A simple system for laser-illuminated video imaging of sediment suspension and bed topography. *IEEE J. Oceanic Eng.* 23 (1), 12-19.
- Davies, A.G., 1985. Field observations of the threshold of sediment motion by wave action. *Sedimentology* 32, 685-704.
- Department of Defence, 2000. *Australian National Tide Tables 2000*. Australian Hydrographic Publs., 18, 282 pp.
- Dingler, J.R., Boyllis, J.C. and Lowe, R.L., 1977. A high frequency sonar for profiling small-scale bedforms. *Mar. Geol.* 24, 279-288.
- Dingler, J.R. and Inman, D.L., 1976. Wave-formed ripples in nearshore sands. *Coastal Eng.* 2109-2126.

- Done, T.J., 1981. Photogrammetry in coral reef ecology: A technique for the study of change in coral reef communities. Fourth Int. Coral Reef Symposium, Manila, pp 315-320.
- Doucette, J.S., in review. Bedform Migration and sediment dynamics in the nearshore of a low-energy sandy beach in southwestern Australia. *J. Coastal Res.*
- Foti, E. and Blondeaux, P., 1995. Sea ripple formation: the heterogeneous sediment case. *Coastal Eng.* 25, 237-253.
- Granshaw, S.I., 1980. Bundle adjustment methods in engineering photogrammetry. *Photogrammetric Record* 10 (56), 181-207.
- Greenwood, B., Raymond, G.R. and Brander, R.W., 1993. Acoustic imaging of seabed geometry: a high resolution remote tracking sonar (HRRTS II). *Mar. Geol.* 112, 207-218.
- Hanes, D.M. and Bowen, A.J., 1985. a granular-fluid model for steady, intense bedload transport. *J. Geophys. Res.* 90 (C5), 9149-9158.
- Hanes, D.M., Vincent, C.E., Huntley, D.A. and Clarke, T.L., 1988. Acoustic measurements of suspended sand concentration in the C²S² experiment at Stanhope Lane, Prince Edward Island. *Mar. Geol.* 81, 185-196.
- Harvey, E.S. and Shortis, M.R., 1996. A system for stereo-video measurement of subtidal organisms. *Mar. Tech. Soc. J.* 29 (4), 10-22.
- Hay, A.E. and Wilson, D.J., 1994. Rotary sidescan images of nearshore bedform evolution during a storm. *Mar. Geol.* 119, 57-65.
- Holland, K. T. and R. A. Holman. 1997. Video estimation of foreshore topography using trinocular stereo. *Journal of Coastal Research*, 13(1), 81-87
- Holland, K.T., Raubenheimer, B., Guza, R.T., and Holman, R.A., 1995. Runup kinematics on a natural beach. *J. Geophys. Res.* 100 (C3), 4984-4993.
- Holman, R.A. and Guza, R.T., 1984. Measuring run-up on a natural beach. *Coastal Eng.* 8, 129-140.
- Holman, R.A. and Sallenger, A.H. Jr., 1985. Setup and swash on a natural beach. *J. Geophys. Res.* 90 (C1), 945-953.
- Inman, D.L., 1963. Sediment: physical properties and mechanics of sedimentation. In: F.P. Shepard (Ed), *Submarine Geology*, Harper and Row, New York, p.557.
- Kachel, N.B. and Sternberg, R.W., 1971. Transport of bedload as ripples during an ebb current. *Mar. Geol.* 10, 229-244.

- Klimley, A.P. and Brown, S.T., 1983. Stereophotography for the field biologist: measurement of lengths and three dimensional positions of free swimming sharks. *Mar. Biol.* 74, 175-185.
- Larsen, L.H., 1982., A new mechanism for seaward dispersion of midshelf sediments. *Sedimentology* 29, 279-283.
- Lettau, K. and Lettau, H.H., 1978. Experimental and micro-meteorological field studies on dune migration. In: H.H. Lettau and K. Lettau (Eds), *Exploring the World's Driest Climate*, University of Wisconsin-Madison, Institute for Environmental Studies, IES Report 101, pp. 110-147.
- Li, M.Z. and Amos, C.L., 1999. Field observations of bedforms and sediment transport thresholds of fine sand under combined waves and currents. *Mar. Geol.* 158, 147-160.
- Li, M.Z., Amos, C.L. and Heffler, D.E., 1997. Boundary layer dynamics and sediment transport under storm and non-storm conditions on the Scotian Shelf. *Mar. Geol.* 141, 157-181.
- Lippmann, T.C. and Holman, R.A., 1989. Quantification of sand bar morphology: a video technique based on wave dissipation. *J. Geophys. Res.* 94 (C1), 995-1011.
- Lippmann, T.C. and Holman, R.A., 1990. The spatial and temporal variability of sand bar morphology. *J. Geophys. Res.* 95 (C7), 11575-11590.
- Lippmann, T.C., Holman, R.A., and Hathaway, K.K., 1993. Episodic, nonstationary behavior of a double bar system at Duck, N.C., U.S.A., 1986-1991. *J. Coastal Res.* SI 15, 49-75.
- Masselink, G. and Pattiaratchi, C., 2000. Tidal asymmetry in sediment resuspension on a macrotidal beach in northwestern Australia. *Mar. Geol.* 163, 257-274.
- Osborne, P.D. and Vincent, C.E., 1993. Dynamics of large and small-scale bedforms on a macrotidal shoreface under shoaling and breaking waves. *Mar. Geol.* 115, 207-226.
- Plant, N.G. and Holman, R.A., 1997. Intertidal beach profile estimation using video images. *Mar. Geol.* 140, 1-24.
- Shi, N.C. and Larsen, L.H., 1984. Reverse sediment transport induced by amplitude-modulated waves. *Mar. Geol.* 54, 181-200.
- Shortis, M.R. and Beyer, H.A., 1997. Calibration stability of the Kodak DCS420 and 460 cameras. *Videometrics V*, SPIE Vol. 3174, pp. 94-105.

- Shortis, M. R., Miller, S., Harvey, E. S. and Robson, S., 2000. An analysis of the calibration stability and measurement accuracy of an underwater stereo-video system used for shellfish surveys. *Geomatics Research Australasia* 73, 1-24.
- Sleath, J.F.A., 1982. The suspension of sand by waves. *J. Hydraul. Res.* 20 (5), 439-452.
- Thornton, E.B., Swaine, J.L. and Dingler, J.R., 1998. Small-scale morphology across the surf zone. *Mar. Geol.* 145, 173-196.
- Villard, P.V., Osborne, P.D. and Vincent, C.E., 2000. Influence of wave groups on SSC patterns over vortex ripples. *Cont. Shelf Res.* 20 (17), 2391-2410.
- Whorff, J.S. and Griffing, L., 1992. A video recording and analysis system used to sample intertidal communities. *Mar. Biol. Ecol.* 160, 1-12.

Fig. 1. Deployed stereo-video system.

Fig. 2. Calibration cube. View from left camera. The white object in the bottom right corner is the LED.

Fig. 3. Port Beach field site.

Fig. 4. Measurement errors as tested on nail heights and positions in a water tank along x, y, and z axes. # of observations denotes the number of repeated measurements of the same distance. Error bars are the standard deviation from the mean error.

Fig. 5. Measurement errors as tested under field condition. Measurements are of distances on the calibration cube along x, y and z axes. # of observations denotes the number of repeated measurements of the same distance. Error bars are the standard deviation from the mean error.

Table 1. Theoretical accuracy and coverage for camera focal length of 3.45mm, camera separation of 0.25m and convergence angle of 8.1° .

Fig. 6. Profile measurements of an artificial rippled surface. The solid line is the actual ripple surface and the dotted line is the surface as measured using the stereo-video system in the water tank.

Fig. 7. Time series of: (a) ripple crest positions; (b) water surface elevation; (c) cross-shore current; (d) suspended sediment concentration.

Fig. 8. Spectra of (a) cross-shore current and (b) ripple crest position. Cospectra of (c) cross-shore current and ripple crest position, and (d) cross-shore current and suspended sediment concentration. In (a) and (b), the solid line denotes spectra for whole data set and the dashed line denotes spectra for a subset of the data set.

Fig. 9. Subset of the data set in Fig. 7. Time series of: (a) cross-shore current; (b) ripple crest positions; (c) low-pass filtered (0.1Hz) cross-shore current (solid line) and ripple crest position (line with x's); (d) high-pass filtered (0.2Hz) cross-shore current (solid line) and ripple crest position (line with x's).

Fig. 10. Time series of: (a) cross-shore current asymmetry for each wave; (b) mean cross-shore current for each wave; (c) cross-shore current skewness for each wave; (d) cross-shore sediment flux at 0.05m above the bed; (e) ripple crest positions. The straight solid line in (a), (b) and (c) is the line of best fit.

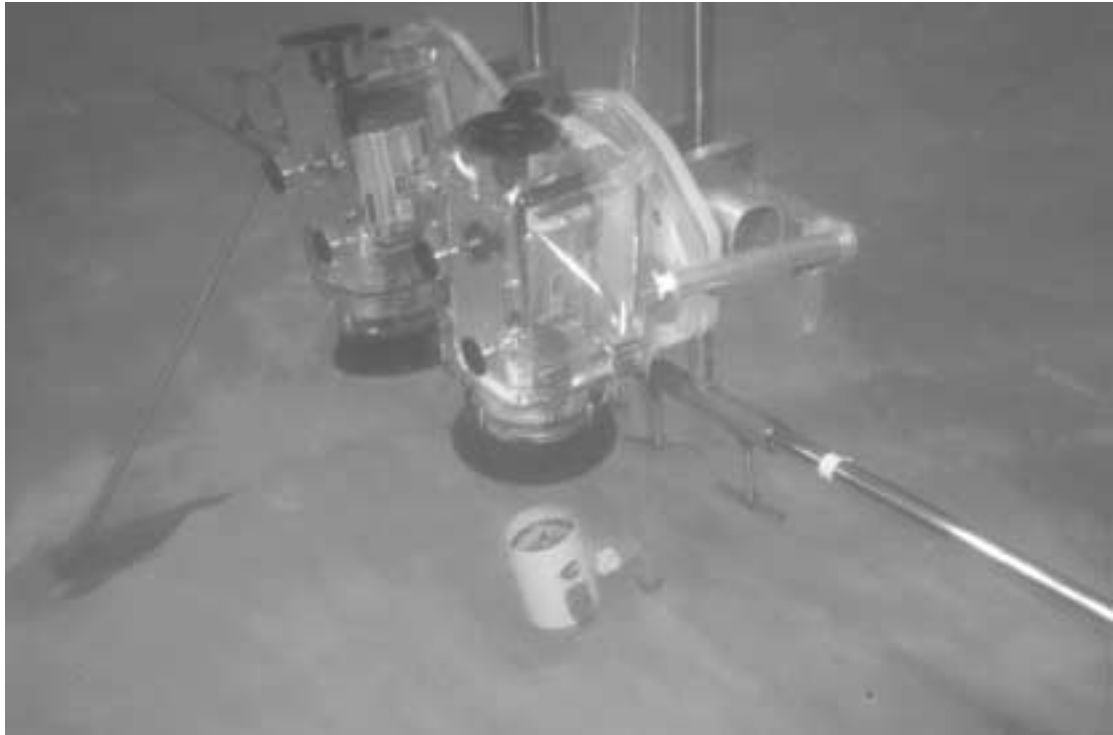


Fig. 1

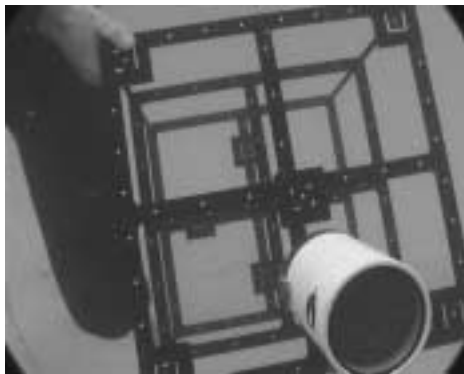


Fig. 2

Table 1

Range m	z precision mm	x and y precision mm	Coverage (m)	
			x	y
0.2	0.1	0.2	0.03	0.15
0.3	0.3	0.2	0.17	0.22
0.4	0.5	0.3	0.31	0.29
0.5	0.8	0.4	0.45	0.37
0.6	1.2	0.5	0.59	0.44
0.7	1.6	0.6	0.73	0.52
0.8	2.1	0.6	0.87	0.59

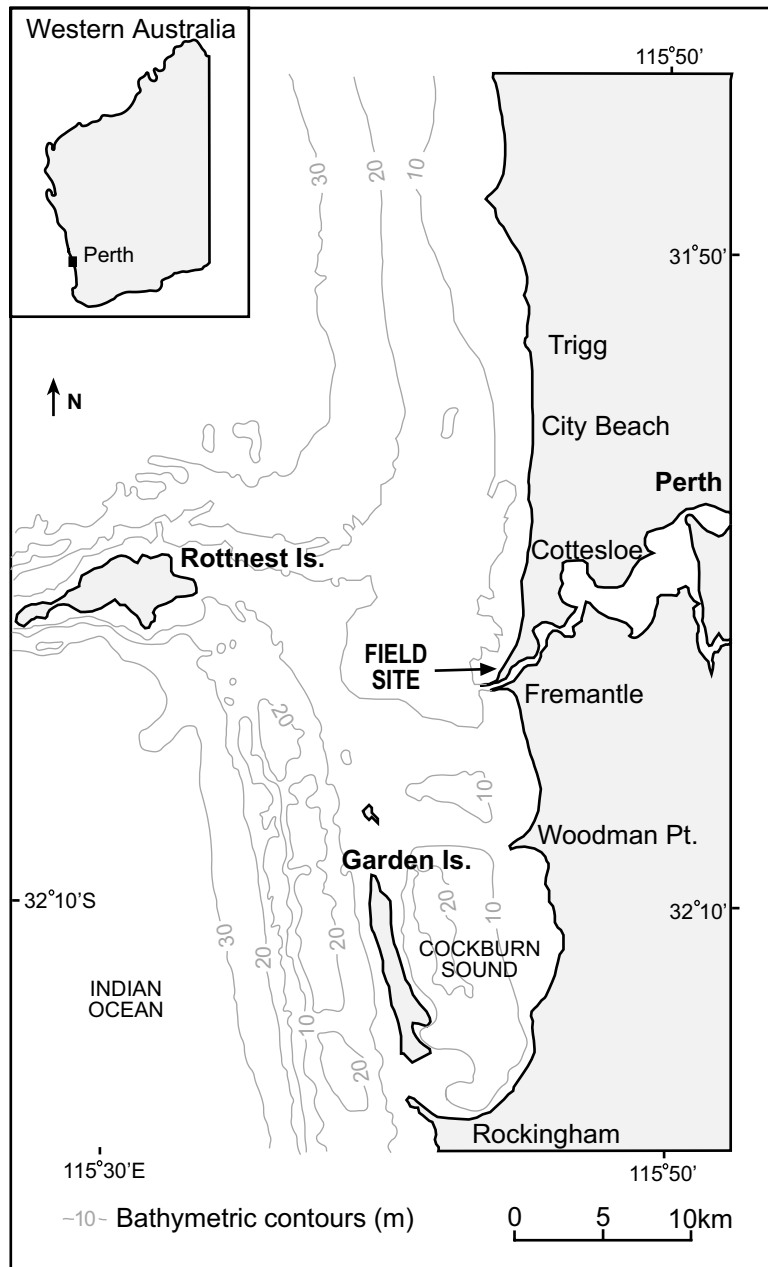


Fig. 3

Fig 3.

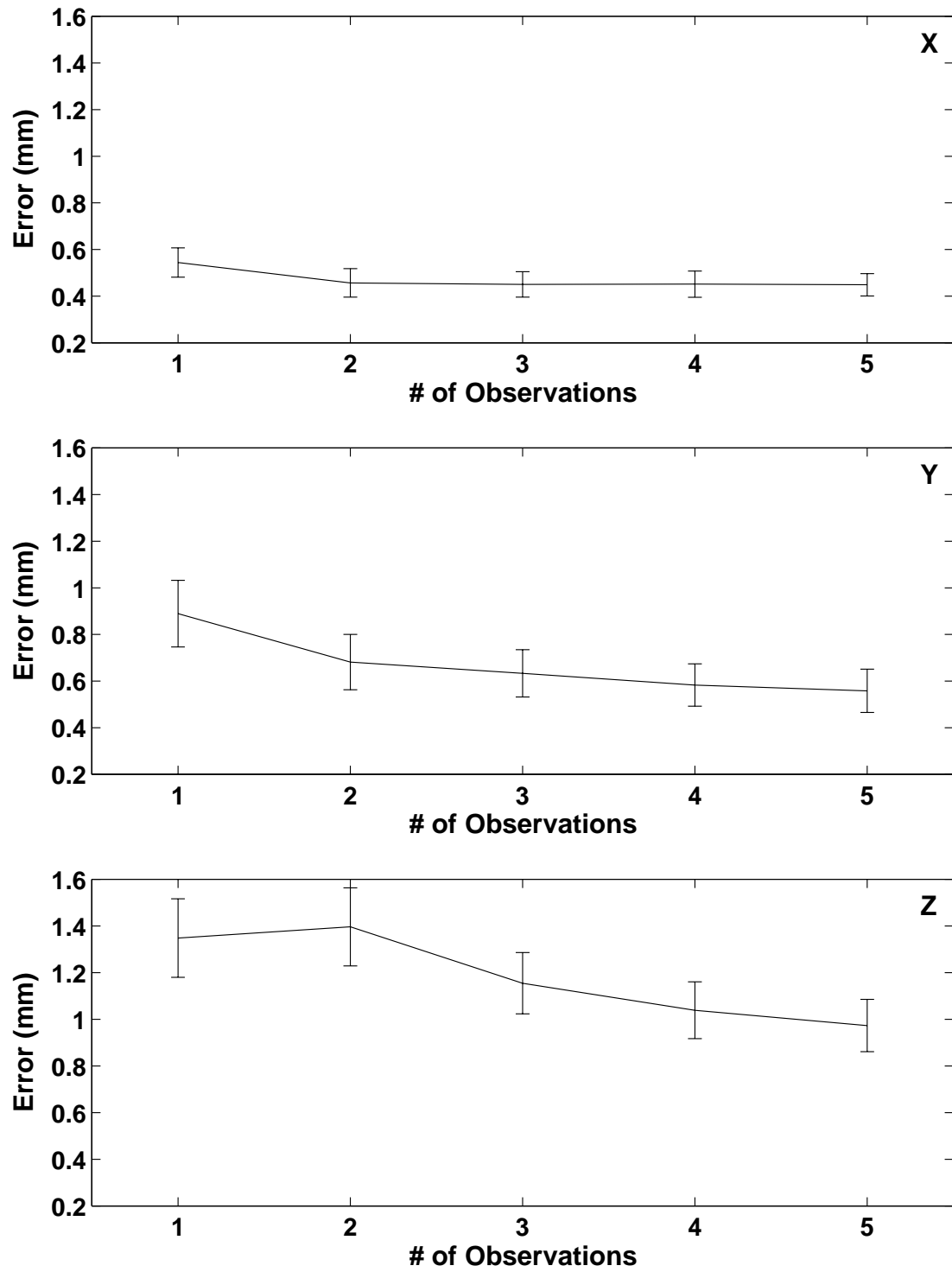


Fig 4.

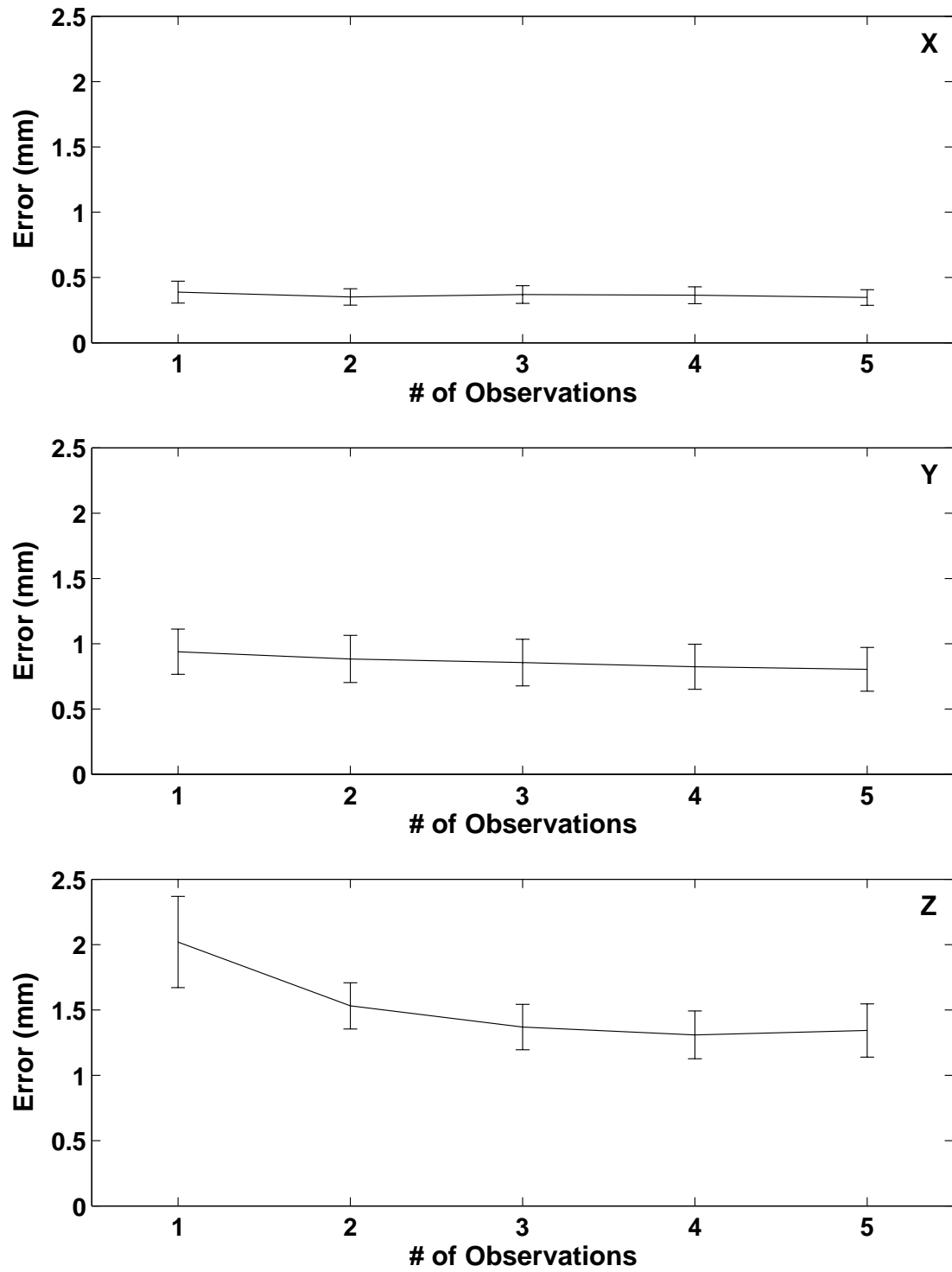


Fig 5.

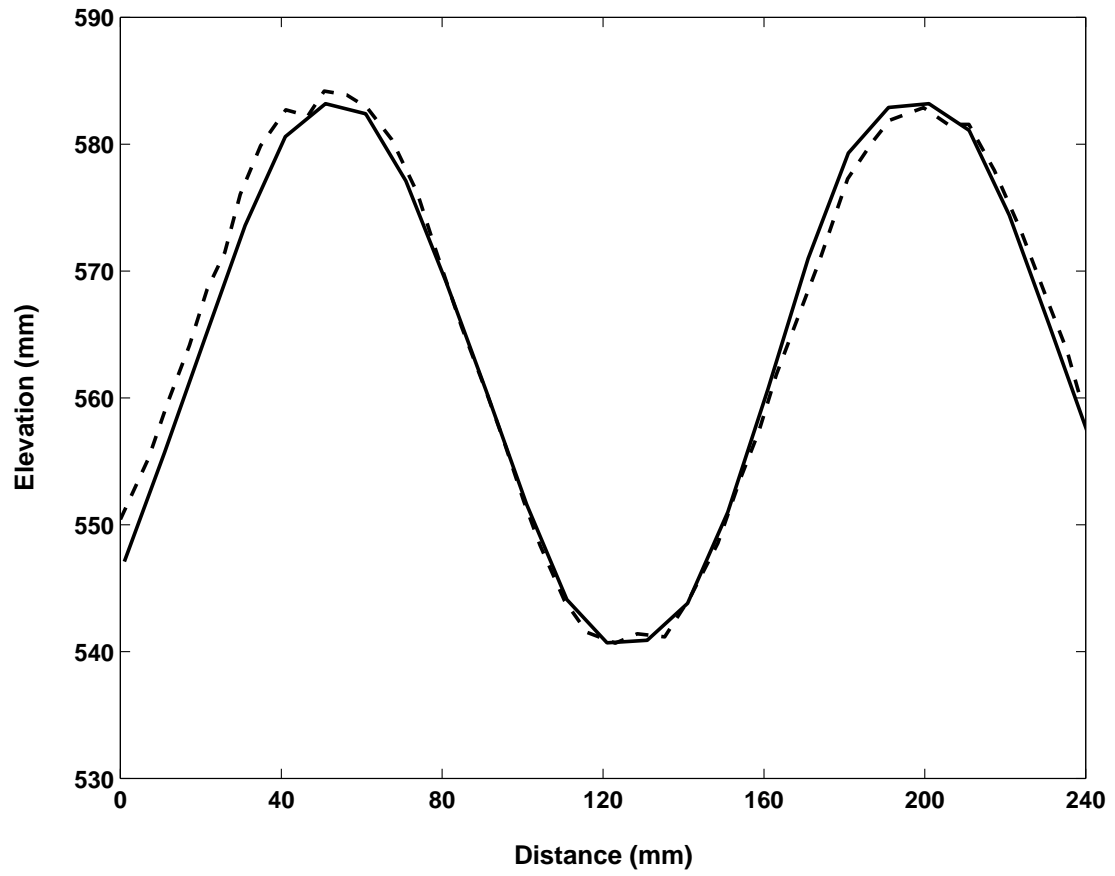


Fig 6.

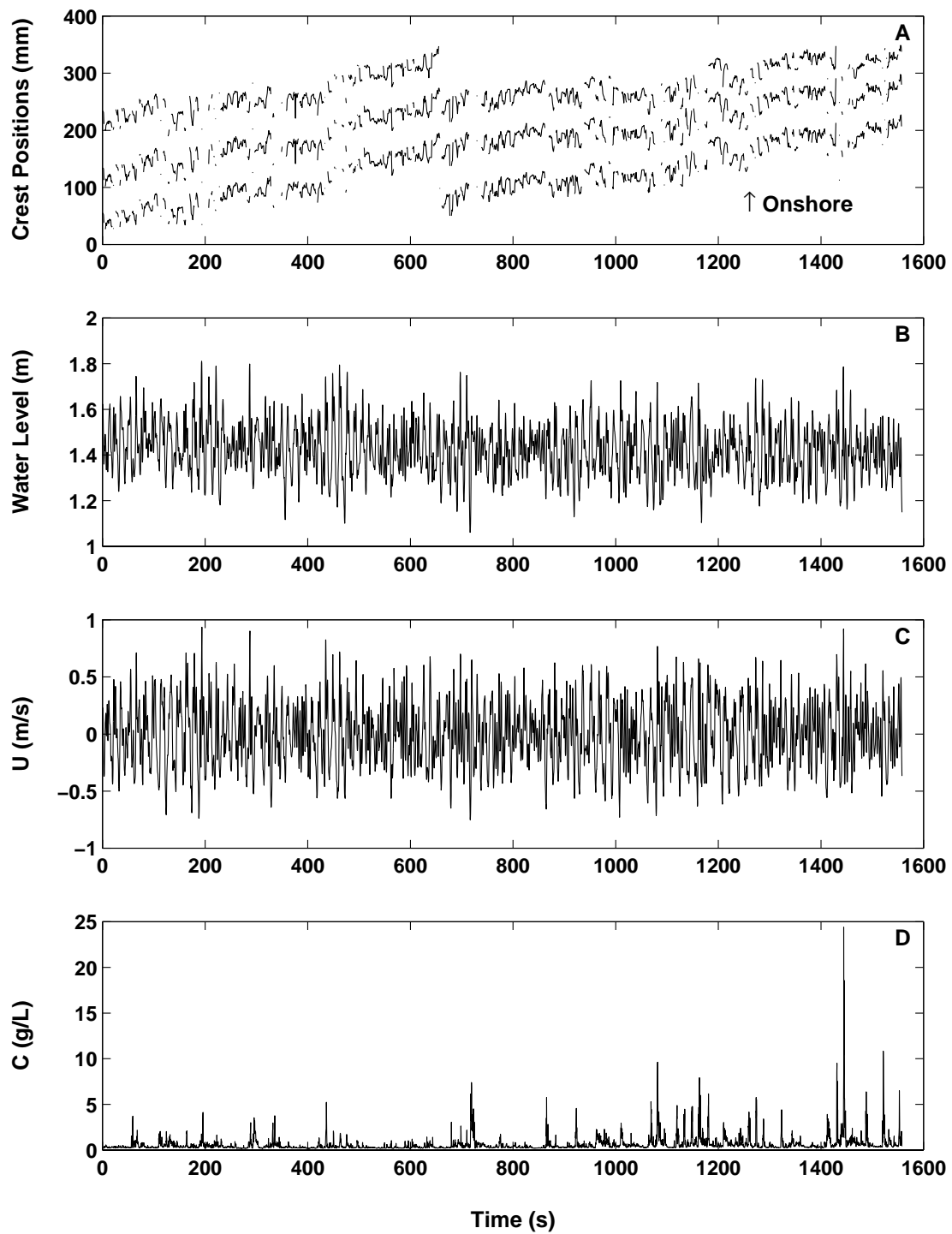


Fig 7.

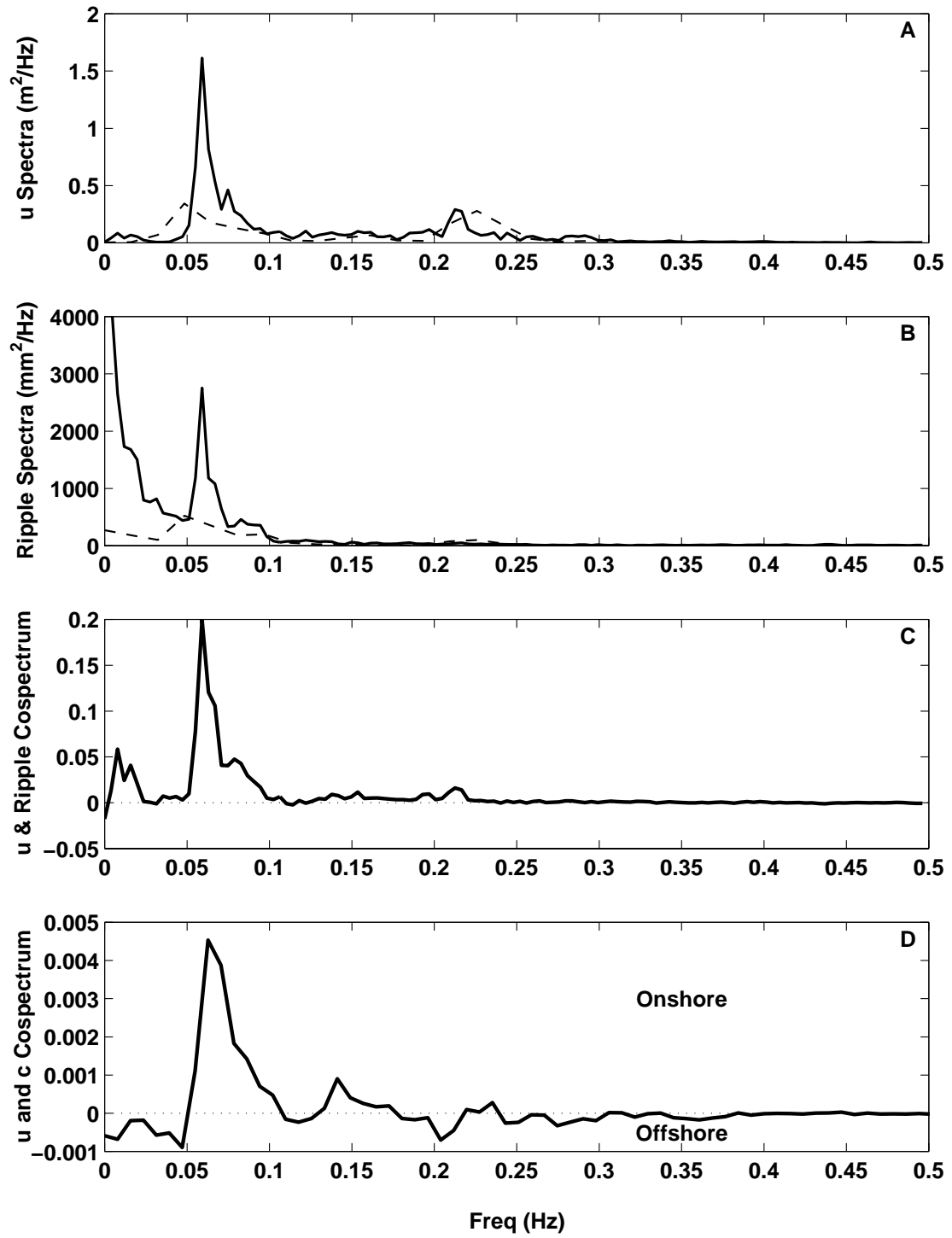


Fig 8.

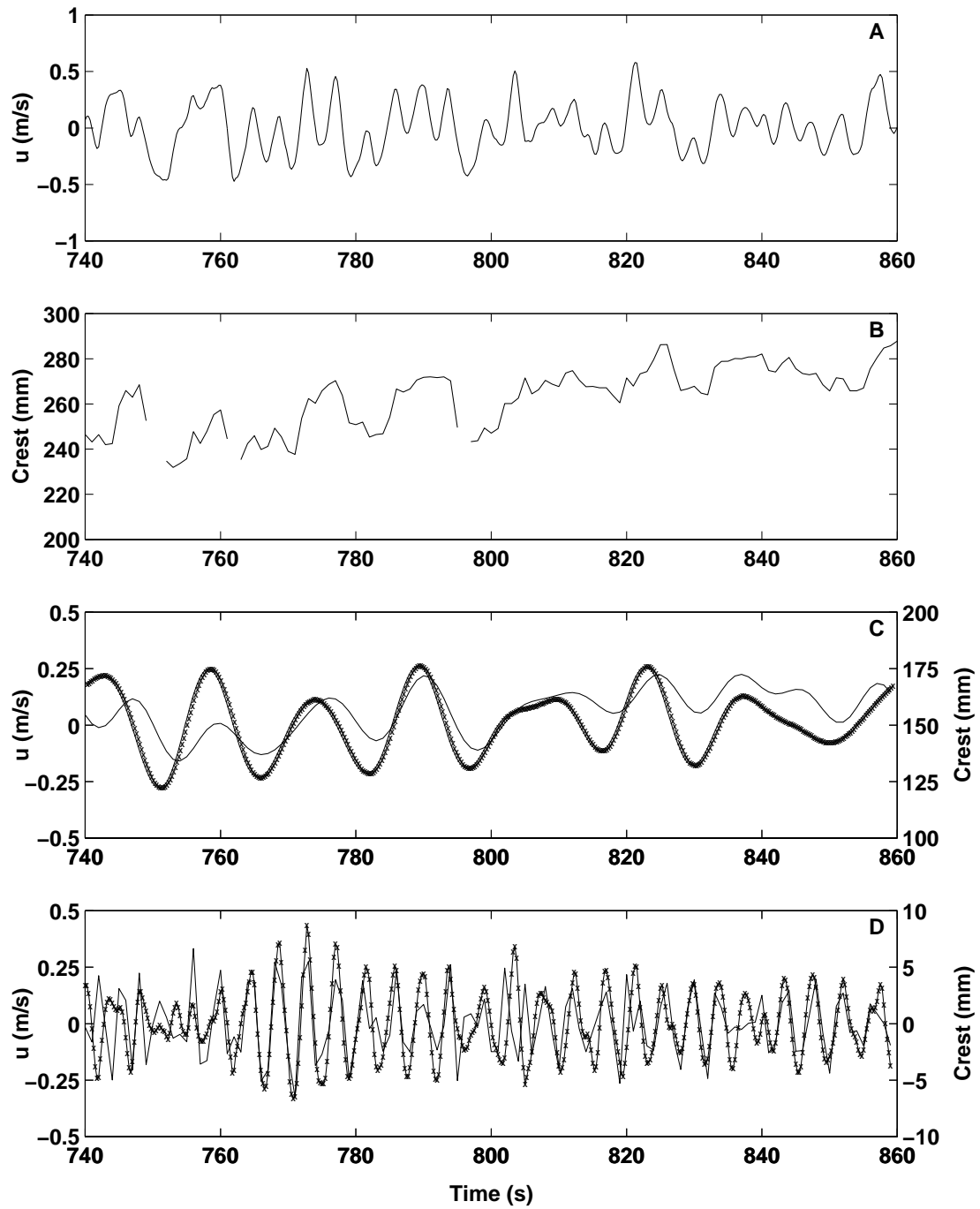


Fig 9.

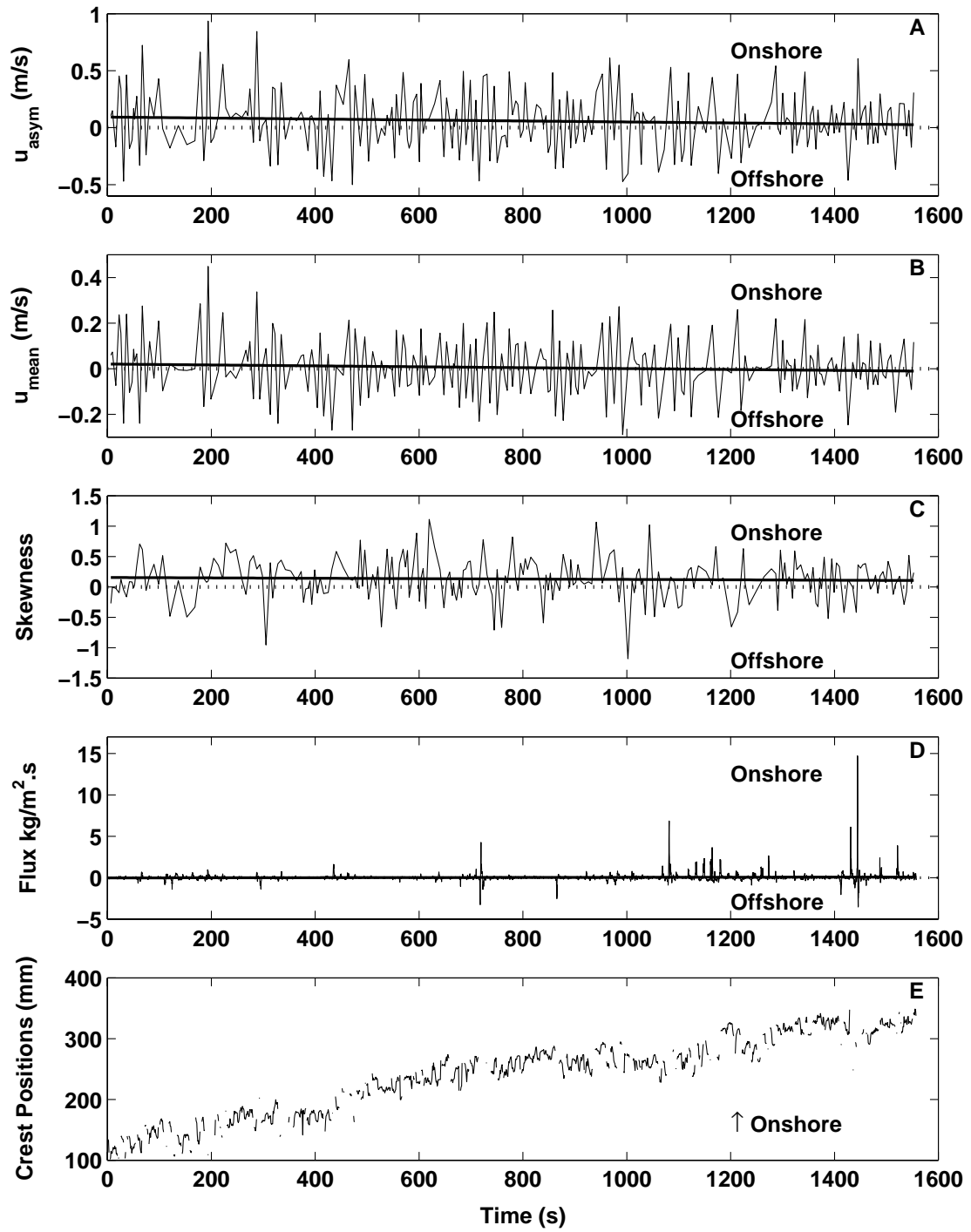


Fig 10.